Characterizing the Optical Nature of the Blazar S5 1803+784 during Its 2020 Flare

A. Agarwal[1] , Ashwani Pandey[2] , Aykut Özdönmez[3], Ergün Ege[4], Avik Kumar Das[1] , and Volkan Karakulak[5]
[1] Raman Research Institute, C. V. Raman Avenue, Sadashivanagar, Bengaluru—560 080, India; aditi.agarwal@rri.res.in
[2] Indian Institute of Astrophysics, Block II, Koramangala, Bangalore, 560034, India
[3] Ataturk University, Faculty of Science, Department of Astronomy and Space Science, 25240, Yakutiye, Erzurum, Turkey
[4] Istanbul University, Faculty of Science, Department of Astronomy and Space Sciences, 34116, Beyazıt, Istanbul, Turkey
[5] Ataturk University, Graduate School of Natural and Applied Sciences, Department of Astronomy and Space Science, 25240, Yakutiye, Erzurum, Turkey

Abstract

We report the results from our study of the blazar S5 1803+784 carried out using quasi-simultaneous B, V, R, and I observations from 2020 May to 2021 July on 122 nights. Our observing campaign detected a historically bright optical flare during MJD 59,063.5−MJD 59,120.5. We also found the source in its brightest ($R_{mag} = 13.617$) and faintest ($R_{mag} = 15.888$) states to date. On 13 nights, covering both flaring and nonflaring periods, we searched for intraday variability using the power-enhanced F-test and the nested ANOVA test. We found significant variability in 2 of these 13 nights. However, no such variability was detected during the flaring period. From correlation analysis, we observed that the emission in all optical bands were strongly correlated with a time lag of ∼0 days. To get insights into its dominant emission mechanisms, we generated the optical spectral energy distributions of the source on 79 nights and estimated the spectral indices by fitting a simple power law. The spectral index varied from 1.392 to 1.911 and showed significant variations with time and R-band magnitude. We detected a mild bluer-when-brighter (BWB) trend during the whole monitoring period and a much stronger BWB trend during the flare. We also carried out a periodicity search using four different methods and found no significant periodicity during our observation period. Based on the analysis during the flaring state of the source one can say that the emissions most likely originate from the jet rather than from the accretion disk.

Unified Astronomy Thesaurus concepts: Blazars (164); BL Lacertae objects (158); Active galactic nuclei (16); Active galaxies (17)

1. Introduction

BL Lacertae objects (weak or no line profile in optical spectra) and flat-spectrum radio quasars (FSRQs) are a violently variable subclass of blazars. Blazars are characterized by high and variable distinctive polarization along with strong and fast flux variability at all wavelengths from radio to γ-rays (Wagner & Witzel 1995; Urry & Padovani 1995). Flux variability in most blazars appears to be unpredictable and few of them have relatively reliable periodic variability (e.g., OJ 287; Valtonen et al. 2008). Blazar variability is generally referred to in three groups: intraday variation (IDV) or microvariability for flux variations up to a few tenths of a magnitude spanning over a few minutes up to a day, short-term variation (STV) for variations exceeding 1 mag on a timescale of a few months, and long-term variation (LTV) for variations of a few magnitudes over a longer timescale (months to many years). However, the trend of long-term light curves may indicate possibly longer recurrent timescales (e.g., Massaro et al. 2001; Gupta et al. 2008). The mechanisms and periodicity underlying these kinds of flux variability are still open questions. Flux variability in blazars could be attributed to the shocks moving along the jet (Marscher & Travis 1996), accretion disk instabilities (Wiita 1996), gravitational microlensing (Schneider & Weiss 1987), or the change of the Doppler factor owing to the emission plasma moving at relativistic speeds along a spiral path (Raiteri et al. 2017). Measuring flux and spectral changes of

blazars using multiband observations is highly valuable as it provides information about the location, size, structure, and dynamics of the radiating region and the cooling timescales of electrons in relativistic jets and also tests theoretical models (e.g., Ciprini et al. 2003; Gupta et al. 2008; Agarwal & Gupta 2015).

Emission from blazars spans the complete EM spectrum, thus allowing us to study them on a wider frequency range extending up to very high energy γ-rays. Blazars display a double-humped structure in their broadband spectral energy distributions (SEDs; e.g., Fossati et al. 1997). The first hump, which is the low-energy component, peaks in the infrared (IR) to X-rays, while the second (high-energy) hump peaks from GeV to TeV frequencies. The synchrotron emission from relativistic particles associated with relativistic jets is attributed to the low-energy part of the SED, while according to the widely accepted leptonic scenarios, the high-energy hump could be due to the inverse Compton (IC) scattering of low-frequency photons by highly energetic particles. However, the origin of the latter component is still a question. Various models have been proposed to understand the high-energy features (e.g., Böttcher 2007). Nonthermal leptonic processes that can explain the second component include the synchrotron self-Compton (SSC) model and the external Compton (EC) model. According to the SSC model (e.g., Mastichiadis & Kirk 2002, and references therein), the IC emission from the population of electrons upscattering low-energy photons is responsible for the high-energy features of the SED. In contrast, according to the EC model, the second hump is due to photons from the ambient medium, e.g., the accretion disk, broad-line region, and dusty torus (Dermer & Schlickeiser 1993; Sikora 1994). In hadronic scenarios, very high energy

γ-rays are produced by a variety of mechanisms such as photopion and photopair interactions, which also generate neutrinos in the process (Mannheim 1993). Both leptonic and hadronic models have shown great success in representing SEDs except in certain scenarios where leptonic models may pose some problems for observed data.

Blazars are further classified based on the location of the synchrotron peak (ν_{syn}) into three subclasses: low synchrotron frequency peaked (LSP) with $\nu_{syn} \leqslant 10^{14}$ Hz, intermediate synchrotron frequency peaked (ISP) with $10^{14} < \nu_{syn} < 10^{15}$ Hz, and high synchrotron frequency peaked (HSP) with $\nu_{syn} \geqslant 10^{15}$ Hz (Abdo et al. 2010). Fan et al. (2016) studied a large sample of blazars and slightly revised the above classification scheme of blazars. According to the authors, LSPs have the same location of the synchrotron peak but ISPs lie in the range $10^{14} < \nu_{syn} < 10^{15.3}$ Hz, whereas HSPs will have $\nu_{syn} \geqslant 10^{15.3}$ Hz. In addition to these subclasses of blazars, a growing subclass has come to light, which is popularly known as extremely high frequency peaked BL Lacertae objects (EHBLs), with the synchrotron peak frequency ranging from medium to hard, i.e., ν_{syn} lying at >1 keV (or $>10^{17}$ Hz; Costamante et al. 2001), and therefore EHBLs are considered to be good candidates for TeV studies.

S5 1803+784 is a BL Lacertae object with a redshift $z = 0.680$ (Lawrence et al. 1996) and a high optical polarization (Cawthorne et al. 2013). S5 1803+784 is a source that has been observed in radio bands and high-energy bands and occasionally in optical bands. It is characterized by strong X-ray and γ-ray radiation and strong flux variation in the entire EM spectrum (see Nesci et al. 2002, 2012; Kun et al. 2018; Nesci et al. 2021). The only systematic optical monitoring was made by Nesci et al. (2002, 2012, 2021) between 1996 and 2021. This long-term monitoring revealed strong flaring activity with large variability. At the same time, analysis of the optical color index versus flux variations revealed minor variations. A recent study by Nesci et al. (2021) demonstrates the lack of any strong correlation between multiband emissions (i.e., radio–optical, optical–X-ray, and X-ray–γ-ray fluxes). A periodic oscillation of the relativistic jet with a period of 6 yr was claimed by Kun et al. (2018) based on analysis of images from very long baseline interferometry. However, Nesci et al. (2002, 2012, 2021) did not find any periodicity in their long-term optical observations.

Since a one-zone SSC model appears too simple to explain the source behavior, Kun et al. (2018) suggested an IC origin for the high-energy emission of the source, nearly co-spatial with the optical region, and radio components originating from the core moving outward, with ejection epochs compatible with those of the two largest γ-ray flares. Active galactic nuclei (AGNs) have diverse radiation mechanisms dominant in various regions; thus, long-term multiwavelength observations are extremely helpful in understanding the complete and detailed picture.

Our fundamental motivation is to analyze the flux and spectral variability of the source in the optical regime on intraday to longer timescales. In this paper, we present the results of quasi-simultaneous optical observations from 2020 May to 2021 July. We captured the source at its historic maxima in $BVRI$ passbands. We also investigated periodicity in the source on longer timescales along with interband correlation. Moreover, we generated the SEDs during 2020–2021. The paper is structured as follows: In Section 2, we outline the properties of the telescopes used for data acquisition along with the data reduction procedure followed. In Section 3, we describe several analysis methods such as a power-enhanced F-test, nested analysis of variance (ANOVA), and variability amplitude analysis. We present our results in Section 4 and finally, discuss the different models and emission mechanisms responsible for the source behavior in Section 5.

2. Observations and Data Reduction

To investigate the optical properties of the blazar S5 1803 +784, we performed quasi-simultaneous observations of the source in $BVRI$ from 2020 May to 2021 July for 122 nights and collected a total of $\sim$2100 $BVRI$ frames.

During our observations, three telescopes were used, namely, the 1.0 m RC (T100) telescope, 60 cm RC robotic (T60) telescope, and 0.5 m RC (ATA50) telescope in Turkey. The technical details of the 1.0 m RC telescope and 60 cm RC robotic telescope are summarized in Agarwal et al. (2021b) while the 0.5 m f/8 RC (ATA50) telescope is located at Ataturk University, Erzurum, and it is equipped with an Apogee Alta U230 2K charge-coupled device (CCD) with a field of view of $26'.3 \times 26'.3$, and standard Johnson BVR and Sloan Digital Sky Survey $ugriz$ filters. A log of our photometric observations, along with the total period of observation on a particular night, is presented in Tables 1 and 2. Photometric images of the target field were taken in the B, V, R, and I passbands in an alternative sequence. Depending on the sky conditions and the brightness of the source, the exposure time ranges from 30 to 300 s.

We used a standard data reduction methodology similar to that in Agarwal et al. (2019), i.e., bias subtraction, twilight flat-fielding, and cosmic-ray removal. After preprocessing the raw images, aperture photometry was carried out to extract the instrumental magnitudes of the blazar and all comparison stars in the source frame using the script we developed with Python and its packages. To find the optimum aperture, we first used different concentric aperture radii of 1.0, 1.2, 1.4, 1.6, 1.8, 2.0, 2.5, and 3.0 times the FWHM of the stars in the field. To subtract the background, the radius of the sky annulus was set to approximately five times the FWHM. The instrumental magnitudes of the blazar and comparison stars in the field were extracted. The field used for our analysis is displayed in Figure 1 (Nesci et al. 2002).

We used the instrumental magnitudes for $1.4 \times$ FWHM of the aperture values with the best signal-to-noise ratio and the minimum standard deviation of the difference between the instrumental magnitudes of the standard stars (the differential magnitudes) for our final analysis.

As emphasized by Cellone et al. (2007), significant differences between the standard stars and blazar might lead to statistically significant yet false detections of microvariability. Keeping this in mind, for calibration of the instrumental magnitudes of the blazar, we used stars A and B from Figure 1, which have brightness closest to that of the blazar.

3. Analysis Techniques

To precisely quantify the variability characteristics in the optical $BVRI$ light curves of the source on diverse timescales, we employed two of the most recent and most powerful statistical methods, namely, the power-enhanced F-test and the nested ANOVA test (de Diego 2014; de Diego et al. 2015). As pointed out by de Diego et al. (2015), various other statistical tests such as the C-test, F-test, and chi-square test, which have been widely used to search for optical variability in the past,

Table 1
Observation Log of S5 1803+784

Date of Observations (yyyy-mm-dd)	Telescope	Number of Data Points				Time Span (∼hr)	Date of Observations (yyyy-mm-dd)	Telescope	Number of Data Points				Time Span (∼hr)
		B	V	R	I				B	V	R	I	
2020-5-13	T100	2	3	218	2	2.36	2020-10-28	T60	2	3	1	2	0.09
2020-5-29	T100	2	2	203	3	1.52	2020-11-2	T60	1	2	1	2	0.09
2020-5-30	T100	2	2	323	2	3.31	2020-11-7	T60	1	1	1	1	0.06
2020-8-2	T60	0	1	1	0	0.01	2020-11-11	ATA50	0	0	2	0	0.07
2020-8-4	T60	1	1	1	1	0.03	2020-11-22	T100	0	0	93	0	2.74
2020-8-5	T60	1	1	1	1	0.03	2020-11-24	T60	3	3	3	3	0.19
2020-8-6	T60	1	1	1	0	0.05	2020-11-25	T60	3	3	3	3	0.44
2020-8-8	T60	1	0	1	1	0.05	2020-11-26	T60	2	2	3	3	0.44
2020-8-11	T60	1	0	1	1	0.05	2020-11-28	T60	3	2	3	3	0.44
2020-8-13	T60	1	0	1	1	0.05	2020-11-29	T60	1	2	0	0	0.15
2020-8-14	T60	1	0	1	1	0.04	2020-12-18	T60	2	2	3	3	0.34
2020-8-16	T60	1	0	1	1	0.05	2020-12-20	T60	3	3	3	3	0.38
2020-8-17	T60	1	0	1	1	0.05	2020-12-24	T60	3	3	2	3	0.37
2020-8-18	T60	1	0	1	1	0.18	2020-12-25	T60	3	3	2	3	0.37
2020-8-19	T60	1	1	1	0	0.15	2020-12-26	T60	3	3	2	3	0.37
2020-8-24	T60	1	1	1	1	0.05	2021-1-4	T60	0	1	1	1	0.08
2020-8-25	T60	1	1	1	1	0.05	2021-1-6	T60	3	2	3	3	0.44
2020-8-27	T60	1	1	0	1	0.05	2021-1-21	T60	3	3	3	3	0.38
2020-8-29	T60	1	1	1	1	0.05	2021-1-22	T60	3	3	3	3	0.38
2020-8-30	T100	0	4	116	2	1.35	2021-1-23	T60	3	3	3	3	0.38
2020-8-30	T60	1	1	1	1	0.05	2021-2-1	T60	2	2	3	3	0.32
2020-8-31	T100	1	1	101	1	1.83	2021-2-11	T100	0	0	79	0	2.31
2020-8-31	T60	1	1	1	1	0.05	2021-5-7	ATA50	0	0	22	0	1.5
2020-9-1	T60	1	0	1	1	0.05	2021-5-14	ATA50	0	0	86	0	3.85
2020-9-3	T60	1	1	1	1	0.15	2021-5-15	ATA50	0	0	25	0	2.44
2020-9-4	T60	1	0	1	1	0.14	2021-5-16	T100	1	2	8	2	0.48
2020-9-5	T60	1	0	1	1	0.14	2021-5-17	ATA50	0	0	09	0	3.11
2020-9-6	T60	1	0	1	1	0.05	2021-5-18	ATA50	0	0	32	0	2.11
2020-9-7	T60	1	0	1	1	0.05	2021-5-19	ATA50	0	0	43	0	3.88
2020-9-8	T60	1	0	1	1	0.05	2021-6-3	T60	1	1	1	1	0.11
2020-9-10	T100	7	11	13	8	2.9	2021-6-4	T60	1	1	1	1	0.08
2020-9-10	T60	1	0	1	1	0.05	2021-6-5	T60	1	1	1	1	0.08
2020-9-11	T60	1	1	1	1	0.06	2021-6-6	T60	1	1	1	1	0.08
2020-9-12	T100	3	3	5	3	0.45	2021-6-7	T60	1	1	1	1	0.08
2020-9-12	T60	1	1	1	1	0.05	2021-6-10	T60	1	1	1	1	0.07
2020-9-13	T100	2	3	4	3	0.36	2021-6-11	T60	1	1	1	1	0.07
2020-9-13	T60	1	1	1	1	0.05	2021-6-12	T60	1	1	1	1	0.07
2020-9-16	T60	1	1	1	1	0.06	2021-6-13	T60	1	1	1	1	0.07
2020-9-17	T60	1	1	1	1	0.06	2021-6-14	T60	1	1	1	1	0.08
2020-9-18	T60	1	1	1	1	0.06	2021-6-18	T60	1	1	1	1	0.08
2020-9-19	T60	1	1	1	1	0.05	2021-6-19	T60	1	1	1	1	0.08
2020-9-25	T60	1	0	1	1	0.05	2021-6-22	T60	2	2	2	2	0.22
2020-9-28	T60	1	1	1	1	0.06	2021-6-23	T60	2	2	2	2	0.22

Note. The columns show (1) the date of observations, (2) the telescope used, (3) the number of data points in each filter on a particular night, and (4) the total hours of observations in each filter. Columns 5, 6, 7, and 8 are the same as Columns 1, 2, 3, and 4, respectively.

have many limitations and caveats, thus causing less reliable results. Analyzing various simulated variable quasars, the authors pointed out that we can attain more reliable results by increasing the number of comparison stars in our analysis. Therefore, we chose the power-enhanced F-test and the ANOVA test, involving multiple comparison stars in the analysis. These two methods are briefly discussed below.

3.1. Power-enhanced F-test

The conventional F-test compares sample variances of the blazar and nonvariable standard stars from the observed frame. In contrast, in the power-enhanced F-test, we take the brightest comparison star as a reference to derive the differential light curves (DLCs) of the blazar and the rest of the comparison stars (e.g., Polednikova et al. 2016; Pandey et al. 2020a, 2020b). The power-enhanced F-statistic is defined as

$$F_{\text{enh}} = \frac{s_{\text{bl}}^2}{s_c^2}, \tag{1}$$

where s_{bl}^2 is the estimated differential variance of the source while s_c^2 represents the combined variance of the comparison stars calculated using Equation (2) of Pandey et al. (2019).

We observed two or more comparison stars with magnitudes close to that of the blazar and in its proximity for this study. We

Table 2
Table 1 Continued

Date of Observations (yyyy-mm-dd)	Telescope	Number of Data Points				Time Span (∼hr)	Date of Observations (yyyy-mm-dd)	Telescope	Number of Data Points				Time Span (∼hr)
		B	V	R	I				B	V	R	I	
2020-9-30	T60	1	1	1	1	0.06	2021-6-25	T60	2	2	2	2	0.22
2020-10-2	T60	0	1	1	1	0.03	2021-6-28	T60	2	2	2	2	0.22
2020-10-3	T60	1	1	1	1	0.06	2021-7-1	T60	2	2	2	2	0.22
2020-10-4	T60	1	1	1	1	0.06	2021-7-5	T60	2	2	2	2	0.27
2020-10-6	T60	0	1	1	1	0.03	2021-7-6	T60	2	2	2	2	0.27
2020-10-7	T60	1	0	0	0	0	2021-7-7	T60	2	2	2	2	0.22
2020-10-9	T60	1	1	1	1	0.05	2021-7-8	T60	2	2	2	2	0.22
2020-10-10	T60	2	2	2	2	0.29	2021-7-9	T60	1	1	1	1	0.08
2020-10-11	T60	2	2	2	2	0.29	2021-7-10	T60	1	1	1	1	0.08
2020-10-12	T100	3	4	4	3	0.54	2021-7-11	T60	1	1	0	1	0.04
2020-10-12	T60	2	2	2	2	0.29	2021-7-12	T60	1	1	1	1	0.08
2020-10-13	T60	2	2	2	2	0.29	2021-7-13	T60	2	1	2	2	0.23
2020-10-15	T60	2	2	2	2	0.29	2021-7-14	T60	1	2	2	2	0.17
2020-10-17	T60	2	2	2	2	0.29	2021-7-15	T60	2	2	2	2	0.23
2020-10-22	T60	0	1	1	1	0.03	2021-7-17	T60	1	1	1	1	0.08
2020-10-24	T60	2	2	2	2	0.12	2021-7-20	T60	1	1	1	1	0.07
2020-10-25	T60	0	0	0	2	0.06	2021-7-21	T60	1	1	1	1	0.08
2020-10-27	T60	2	2	2	1	0.12	2021-7-30	T60	1	1	1	1	0.07

selected the brightest one as the reference for these comparison stars and the remaining (k) ones as the comparison stars. Since the blazar and the comparison stars are from the same observation frame, they share the same number of observations (N) on any particular night; thus, the degrees of freedom (DOFs) for the above expression are given as $\nu_{bl} = N - 1$ and $\nu_c = k(N - 1)$, respectively. The critical F-value ($F_{critical}$) at the 99% confidence level was calculated. The values derived from the F-statistic with $\nu_{bl} = N_{bl} - 1$ DOF in the numerator and $\nu_c = k(N_{bl} - 1)$ DOF in the denominator were compared to the $F_{critical}$ value. A particular light curve was marked variable if $F_{enh} \geqslant F_{critical}$, and nonvariable otherwise.

3.2. Nested ANOVA Test

Nested ANOVA is a highly robust method to check the variability in blazars' light curves. All comparison stars from the field are used as a reference to extract the DLCs of the target blazar (de Diego et al. 2015). An ANOVA test compares the dispersion within different data groups and between groups drawn out from observations of a single object. Unlike the power-enhanced F-test, the ANOVA test used no comparison star, thereby increasing the number of stars to be used for our analysis. The DLCs of the blazar were grouped into different temporal groups such that each group contained five points. We then calculated the mean square due to groups (MS_G) and also the mean square due to nested observations in groups ($MS_{O(G)}$), which were used to estimate the F-statistic as follows (e.g., de Diego et al. 2015; Pandey et al. 2019):

$$F = \frac{MS_G}{MS_{O(G)}}. \tag{2}$$

The null hypothesis was rejected and the light curve was considered variable (V) if the F-value exceeded the critical value $F_{\nu_1,\nu_2}^{(\alpha)}$ at a significance level of 99% ($\alpha = 0.01$); else it was marked nonvariable (NV). Here, the two DOFs, i.e., ν_1 and ν_2, are defined as $a - 1$ and $a(b - 1)$, respectively, where a is the number of groups and b is the total number of observations in the sample.

Using multiple statistical tests to search for variability in AGNs can further increase the reliability of the analysis. Therefore, to ascertain the variability characteristics of our source on intraday timescales, we adopted the above two criteria. A light curve was marked variable if both tests could detect significant variability for $\alpha = 0.01$.

3.3. Amplitude of Variability

To quantify the variation of the light curves on any given night, we used the variability amplitude, which is defined as follows by Heidt & Wagner (1996):

$$A = \sqrt{(A_{max} - A_{min})^2 - 2\sigma^2} \tag{3}$$

where A_{max} and A_{min} are the maximum and minimum differential instrumental magnitudes in the respective blazar light curve while σ represents the mean error.

4. Results

4.1. Flux Variability

An exhaustive and detailed search for blazar variability at different wavelengths is necessary to understand the size and/or location of the emission region and the involved particle acceleration mechanisms and radiative processes. For IDV studies, we considered only those nights when observations were carried out for a minimum of 1 hr so that we had enough photometric data points to detect variability. We have 13 IDV nights with more than 1 hr of observations in the R band following this criterion. Visual inspection of these intraday light curves hints toward the presence of variability on some occasions. Therefore, to statistically characterize IDV during these 13 nights, we used the power-enhanced F-test and the ANOVA test as described in Section 3. Of these 13 nights, the blazar S5 1803+78 was variable on only two nights, i.e., on 2020 May 30, and 2020 November 22, with the amplitude of variability reaching 7.47 and 10.10, respectively. During the remaining 11 nights, light curves show no or very few
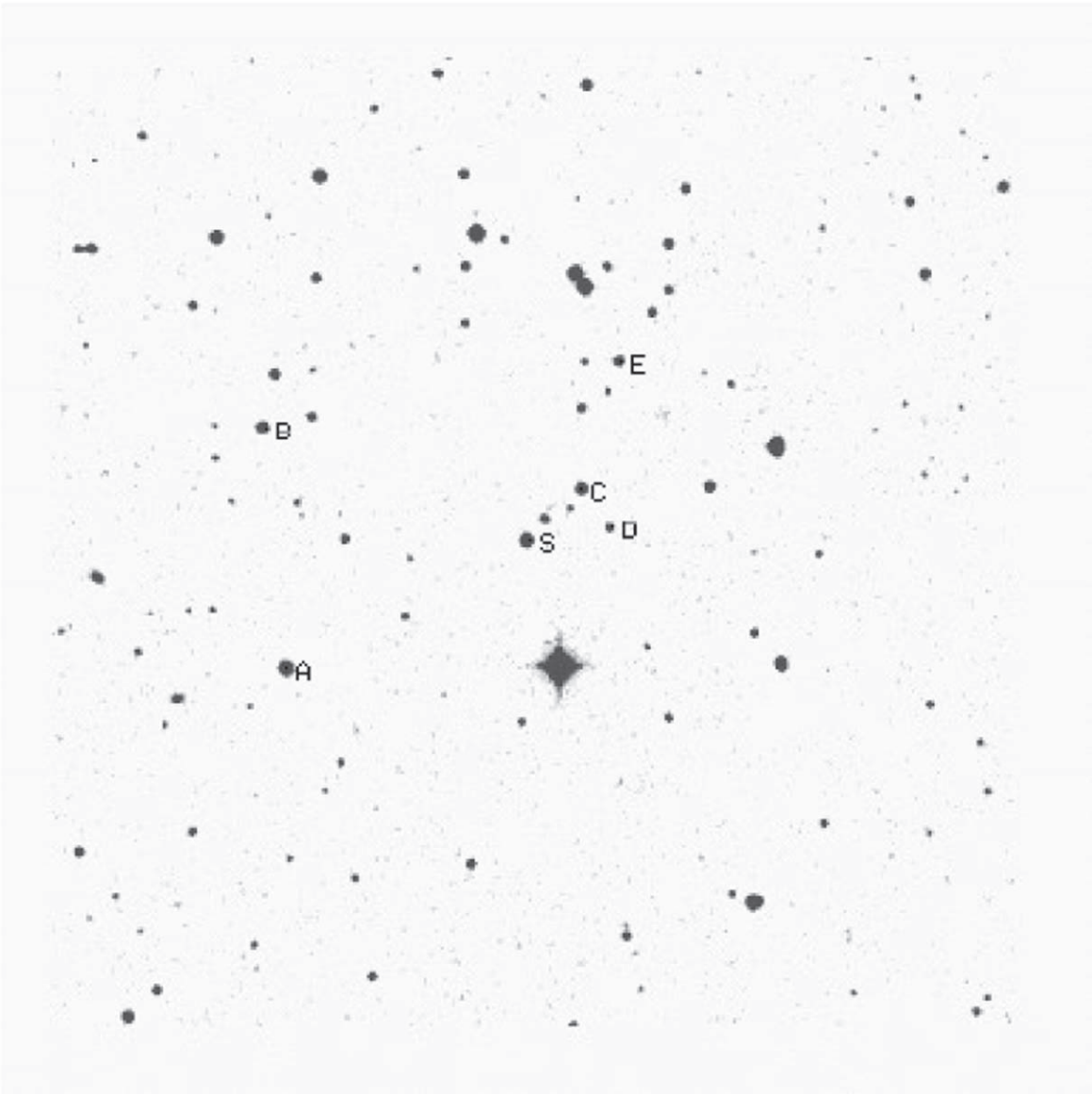
Figure 1. Finding chart of S5 1803+784, where S denotes the blazar and A, B, C, D, and E are the standard stars observed from the frame.

fluctuations. The results of IDV analysis are summarized in Table 3. The calibrated optical R-band IDV light curves of our source S5 1803+78 are shown in Figure 2.

We observed the blazar from 2020 May to 2021 July, long enough to search for LTV. The optical B-, V-, R-, and I-band LTV light curves of our source during the abovementioned period are shown in Figure 3. We shifted the B-, V-, and I-band light curves with respect to the R band by +1.0, +0.5, and −0.5 mag, respectively, to make the long-term light curves more clearly visible. Offsets applied for the same are mentioned in the plot.

On months to years timescales, the optical $BVRI$ light curves of the blazar show large flux variations. Based on the optical data spanning the period from 2020 May to 2021 July, we found a flaring period for the blazar S5 1803+78. As depicted in Figure 3, the flare started from ∼MJD 59,063.5 (2020 August 2) and ended around MJD 59,120.5 (2020 September 28) spanning a period of 57 days. The blazar S5 1803+78 was in the brightest state on 2020 August 25, $B_{mag} = 14.662$,

$V_{mag} = 14.088$, $R_{mag} = 13.617$, and $I_{mag} = 13.033$, while the faintest state of the source was detected on 2020 December 18, with B, V, R, and I brightness values of 17.047, 16.436, 15.888, and 15.198, respectively. The faintest flux level as reported by Nesci et al. (2021) was on 2015 March 18, with the flux in the R band ∼15.0 mag whereas we report an R-band flux of 15.888, which is even fainter by ∼0.89 mag. The maximum flux state identified for this source has been reported by Nesci et al. (2021) with an R-band magnitude of 13.7 on 2016 December 6. Therefore, the flare observed during our monitoring period on 2020 August 25 marks the brightest state of the blazar S5 1803+78 with an R-band magnitude of 13.617. For our entire monitoring period, we also estimated the average $BVRI$ magnitudes of S5 1803+784, which are as follows: the average B magnitude is 16.138, the V magnitude is 15.568, the R-band magnitude is 14.437, and the I-band magnitude is 14.373. The percentage of variation in the amplitude of the source over the entire monitoring period was found to be 238.481%, 234.842%,
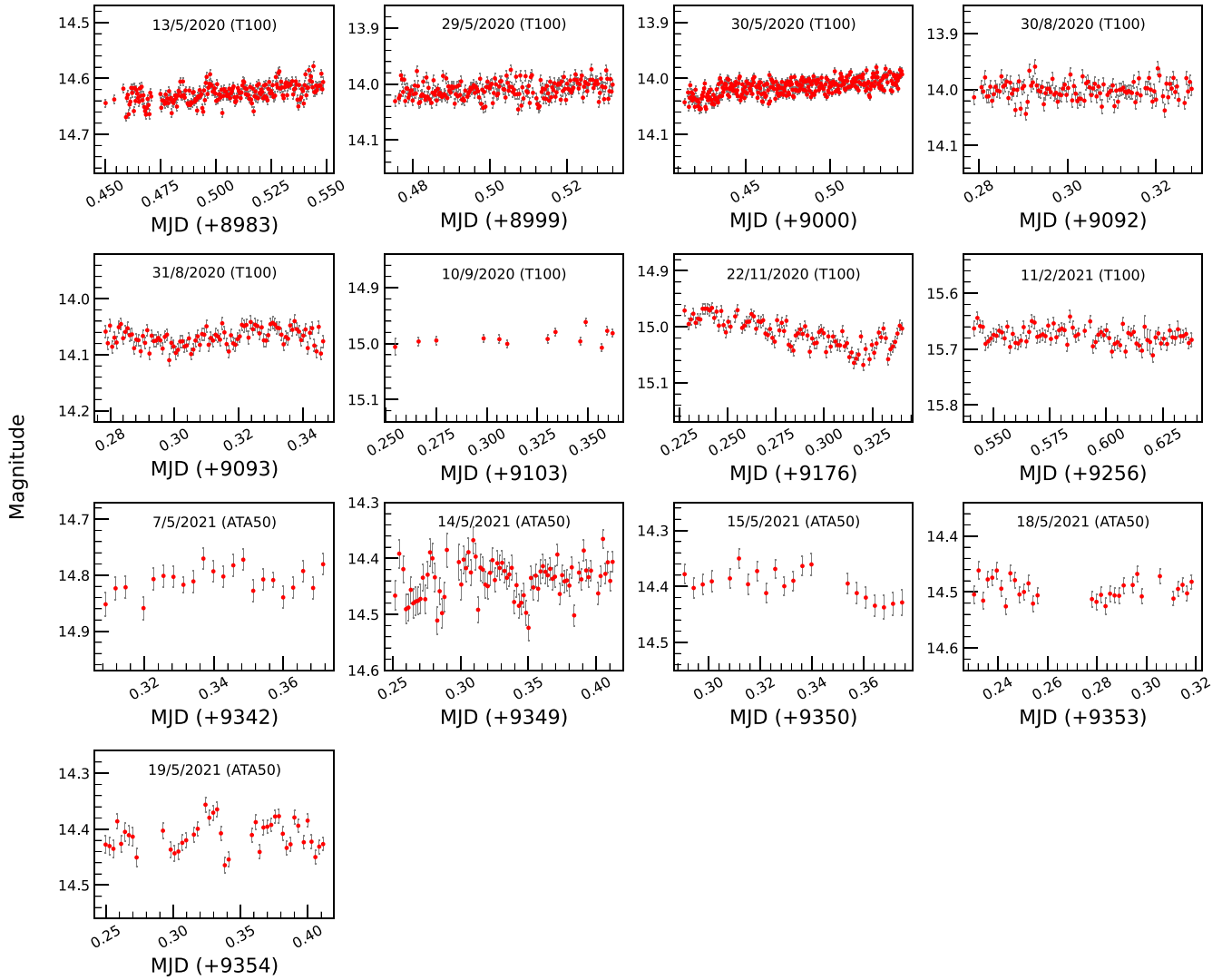
Figure 2. Optical *R*-band intraday light curves for S5 1803+784. The date of observation and the telescope code are written at the top of each plot.

Table 3
Results of IDV Analysis of S5 1803+78

Obs. Date mm-dd-yyyy	MJD	Power-enhanced *F*-test			Nested ANOVA			Status	Amplitude (%)
		DOF (ν_1, ν_2)	F_{enh}	F_c	DOF (ν_1, ν_2)	F	F_c		
5-13-2020	58,982	215, 215	1.00	1.37	42, 172	2.92	1.70	NV	⋯
5-29-2020	58,998	196, 196	1.26	1.40	38, 156	1.54	1.74	NV	⋯
5-30-2020	58,999	317, 317	2.66	1.30	62, 252	4.80	1.55	V	7.47
8-30-2020	59,091	114, 114	1.23	1.55	22, 92	0.75	2.04	NV	⋯
8-31-2020	59,092	99, 99	1.52	1.60	19, 80	5.54	2.14	NV	⋯
9-10-2020	59,102	12, 12	0.71	4.16	1, 8	3.21	11.26	NV	⋯
11-22-2020	59,175	90, 90	3.70	1.64	17, 72	12.77	2.23	V	10.10
2-11-2021	59,256	77, 77	0.77	1.71	14, 60	1.46	2.39	NV	⋯
5-7-2021	59,341	21, 21	0.79	2.86	3, 16	3.44	5.29	NV	⋯
5-14-2021	59,348	82, 82	1.61	1.68	15, 64	3.65	2.33	NV	⋯
5-15-2021	59,349	20, 20	1.88	2.94	3, 16	4.49	5.29	NV	⋯
5-18-2021	59,352	31, 31	1.22	2.35	5, 24	0.99	3.90	NV	⋯
5-19-2021	59,353	42, 42	0.71	2.08	7, 32	2.55	3.26	NV	⋯

227.060%, and 216.566% for *B*, *V*, *R*, and *I*, respectively. The above results are summarized in Table 4. Most interestingly, the data analyzed here do not show strong minute-scale variations even during the flaring state of the target. On the other hand, large amplitude variations were found on STV/LTV timescales, implying that the observed variability trend could be governed by emission regions of sizes similar to STV/LTV timescales.
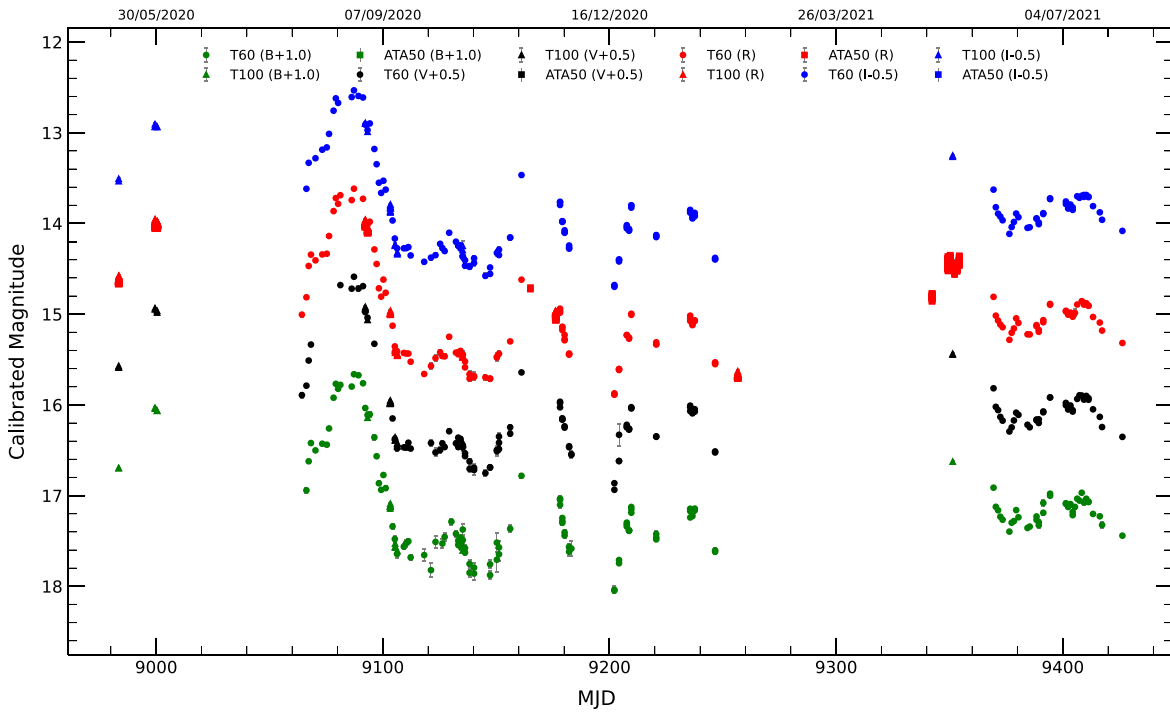
Figure 3. Long-term light curves of S5 1803+784 in *B*, *V*, *R*, and *I* bands.

Table 4
Results of LTV Analysis of S5 1803+78

Band	Brightest Magnitude/MJD	Faintest Magnitude/MJD	Average Magnitude	Variability Amplitude (%)
B	$14.662 \pm 0.018/59{,}086.76861$	$17.047 \pm 0.028/59{,}201.66517$	16.138 ± 0.002	238.481
V	$14.088 \pm 0.011/59{,}086.76972$	$16.436 \pm 0.013/59{,}201.66785$	15.568 ± 0.002	234.842
R	$13.617 \pm 0.009/59{,}086.77027$	$15.888 \pm 0.015/59{,}201.65714$	14.437 ± 0.000	227.060
I	$13.033 \pm 0.009/59{,}086.77073$	$15.198 \pm 0.012/59{,}201.67119$	14.373 ± 0.001	216.566

4.2. Cross-correlation Analysis and Periodicity Search

To quantify any correlations between the optical–optical emission and to estimate possible lags, we used the discrete correlation function (DCF) technique, which was first introduced by Edelson & Krolik (1988) and later used by many other authors (Hovatta et al. 2007; Agarwal & Gupta 2015; Pandey et al. 2017; Acciari et al. 2021, and references therein). One of the advantages of the DCF is that it accounts for irregular sampling of the data set. When light curves are compared with themselves, we get discrete autocorrelations (DACFs). The DACF of each light curve is used to determine if the peaks are obtained due to a lag between different frequencies or indicate the presence of quasiperiodicity within each light curve.

To consider the effects due to densely sampled intraday light curves, we nightly binned the data set. In this regard, we obtained the magnitudes for those nights by taking the weighted average. We also took the mean of the corresponding MJDs. Finally, we performed DCF analysis on various optical–optical light curves for the entire observational period. The plots for the same are displayed in Figure 4. We found a strong correlation between all possible combinations of the optical light curves with a time delay of ∼0 days. The above result was dominant for the whole observation period and also during the enhanced activity in the source during the period ∼MJD 59,063.5 (2020 August 2) to MJD 59,120.5 (2020 September 28). The optical DCFs during the flare are shown in Figure 4.

To search for quasiperiodicity in the source, we used a large number of analysis techniques (Foster 1996; Agarwal et al. 2021a, and references therein), e.g., structure function (SF), DACF, weighted wavelet Z-transform (WWZ), and Lomb–Scargle periodogram (LSP). For the DACF, we considered the detection to be significant if the DACF values were greater than 0.5. DACFs indicate the presence of nonzero side peaks on a timescale of a few days but with values smaller than 0.5. On the other hand, for robust estimation of periodicity using the SF, WWZ, and LSP, we generated a large number of light curves following Timmer & Koenig (1995). Using these simulated light curves, we then estimated the significance of the quasiperiodic oscillation detected using the above three methods. All of the above tests confirm the absence of any clear periodic variability in the optical light curves of the blazar S5 1803+784. The results from the above analysis are displayed in Figure 5.

4.3. SED

To better understand the spectral variations in our source, we extracted the multiband optical SEDs for all those dates when we had quasi-simultaneous observations in all four bands. For this, it was necessary to correct the calibrated *BVRI* fluxes for Galactic extinction (A_λ), taken from the NASA/IPAC Extragalactic Database[6]: $A_B = 0.190$ mag, $A_V = 0.143$ mag, $A_R = 0.113$ mag,
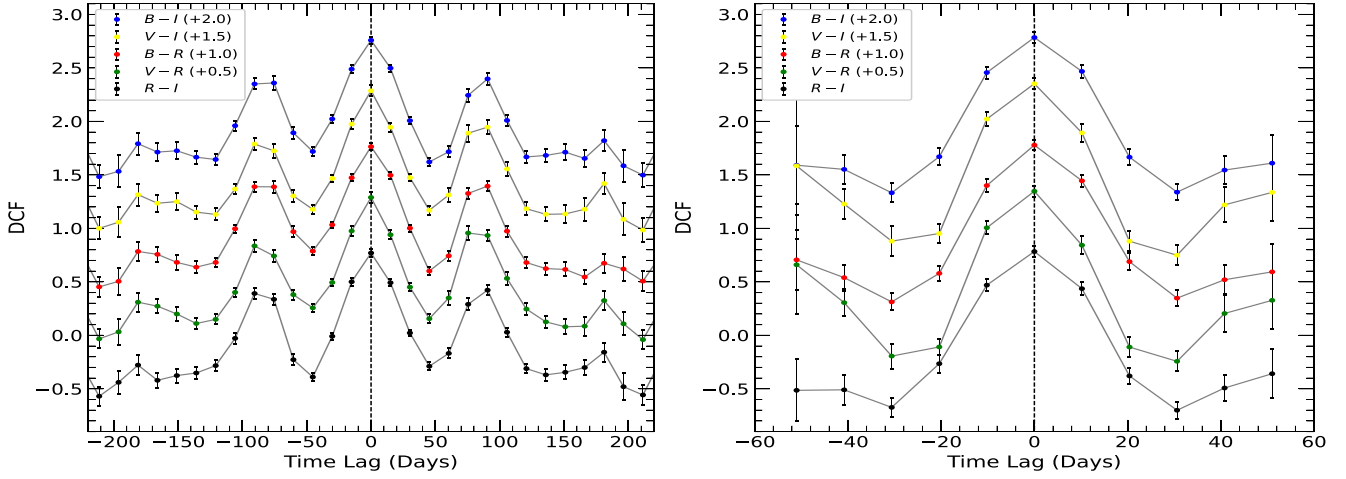
---

[6] https://ned.ipac.caltech.edu/

Figure 4. Cross-correlation analysis for *B*, *V*, *R*, and *I* bands using DCF for the entire monitoring period (left) and for the flaring period (right).
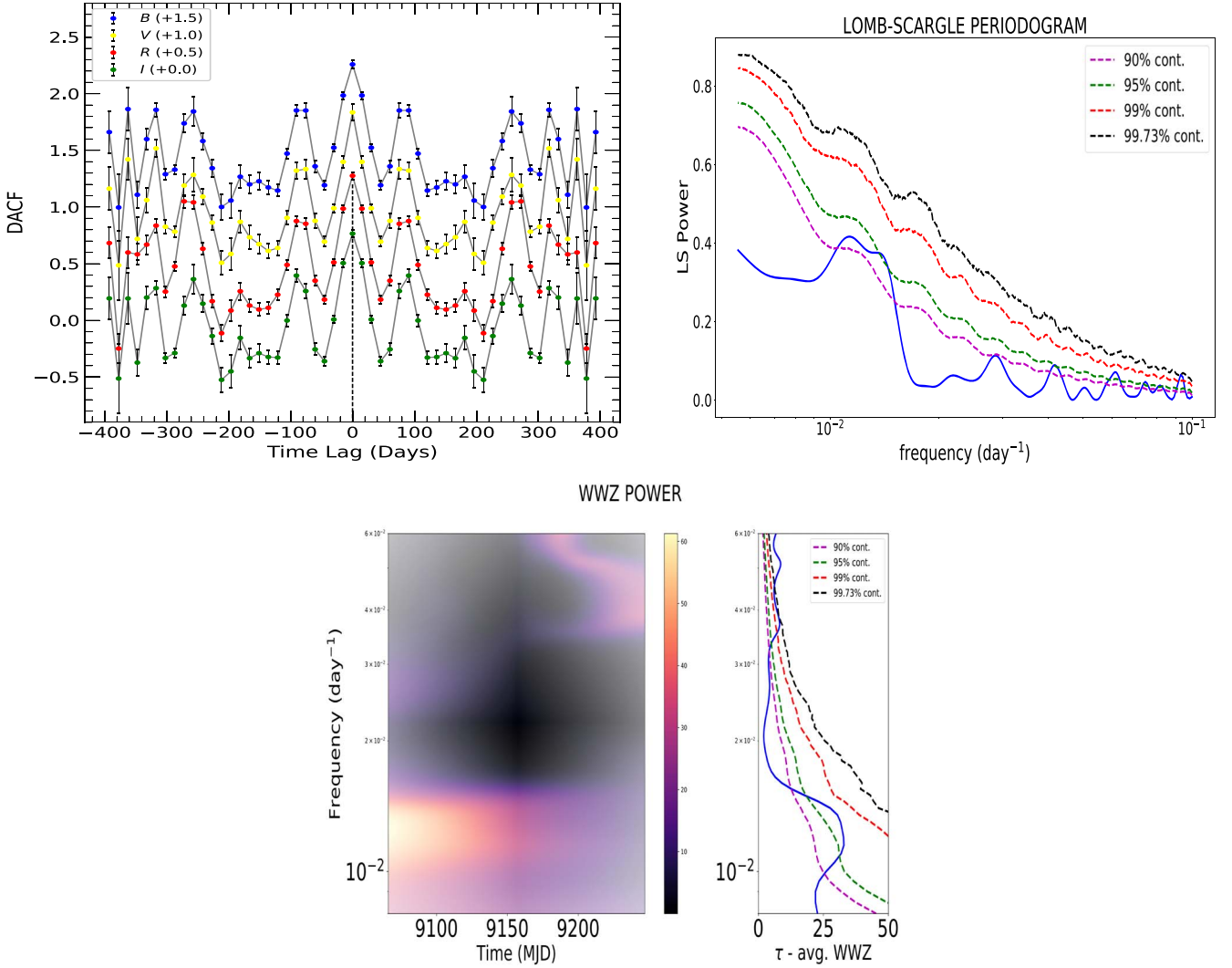

Figure 5. DACF for *B*, *V*, *R*, and *I* bands (top left), LSP for *B* band (top right), and WWZ for *B* band (bottom) for the entire monitoring period.

and $A_I = 0.079$ mag. These corrected magnitudes in the *B*, *V*, *R*, and *I* bands were then converted to the corresponding fluxes following Bessell et al. (1998). We did not apply any subtraction of the host galaxy component from our optical fluxes for the following reasons: (1) The host galaxy of S5 1803+784 could not be resolved/decomposed from deep imaging data (Pursimo et al. 2002). Since the blazar S5 1803 +784 is a point source in our optical images, two-dimensional

decomposition such as by the software package Galfit (Peng et al. 2002) cannot be applied for subtraction from images. (2) The ratio between the core and extended flux densities of S5 1805 calculated from optical and near-IR spectra (Rector & Stocke 2001) is only ∼4%. (3) The contribution of the host galaxy varies by the seeing (equal to the aperture size), and the seeing (and thus the aperture) differs from $1''$ to $3''$ throughout our observation period. This causes an uncertainty in subtraction of the host galaxy flux, typically about a 10%–20% error (Nilsson et al. 1999). (4) In previous optical studies (Nesci et al. 2002, 2021) host galaxy subtraction was not performed as the Ca II break was undetectable or likely negligible in spectra published in previous studies (Lawrence et al. 1996; Rector & Stocke 2001). All of these reasons imply that the contribution of the host galaxy is negligible and cannot be accurately obtained from our optical data.

We have 79 nights with simultaneous $BVRI$ data sets and the optical SEDs for S5 1803+784 on those 79 nights are displayed in Figure 6. The optical SEDs are well defined by a simple power law ($F_\nu = A\nu^\alpha$, where α is the optical spectral index). To derive the spectral indices during these 79 nights, we fitted each SED with a straight line of the form $\log(F_\nu) = -\alpha \, \log(\nu) + C$. The results from these linear fits are given in Table 5. As evident from this table, the spectral index during our observation campaign varies from 1.392 to 1.911 while the weighted mean spectral index is 1.673 ± 0.002, which is in good agreement with Lawrence et al. (1996) and Nesci et al. (2021) and references therein.

In the case of blazars, flux changes can be attributed to color variations, and studying these variations can aid one in understanding the underlying emission mechanism. Two different color trends dominant in blazars are bluer-when-brighter (BWB) and redder-when-brighter (RWB). BL Lacertae objects generally display a BWB trend while FSRQs show an RWB trend, but in some blazars, no clear color behavior has been observed (Böttcher et al. 2009; Agarwal et al. 2015). Moreover, it has been found that the same source displays both these behaviors during different flux states (Wu et al. 2011). To investigate the color behavior of the blazar S5 1803+78, we studied the variation of the spectral index with time and R-band magnitude; we plotted the values of the spectral index given in Column 2 of Table 5 versus time (the left panel of Figure 7) and the R-band magnitudes (the right panel of Figure 7). We fitted straight lines ($S = mV + c$) on the plots of spectral index, S, against R magnitude and S versus time. The values for the slope, m, along with the constant, c, derived from these fits, are listed in Table 6. A positive slope implies a positive correlation between the two quantities, which signifies that a BWB or redder-when-fainter trend is dominant, whereas a negative correlation is observed when we get a negative slope, which implies an RWB behavior.

A large value of the null hypothesis probability (p) implies a higher chance of correlation caused by random noise. In contrast, a smaller p-value suggests a high probability of genuine correlation. A significant positive correlation (a null hypothesis probability $p \leqslant 0.05$) in both plots indicates that the blazar displays a mild BWB trend on longer timescales; thus, the spectrum of the source hardens as the flux increases. We also examined the variation of spectral indices with respect to the R-band magnitude and time only during the flaring period (MJD 59,085.77–MJD 59,111.77) and found similar trends. The straight-line fits of the spectral index versus R magnitude

and time during the flare are displayed in Figure 8 while the results of the straight-line fits are given in Table 7.

5. Discussion and Conclusion

In this paper, we present a set of results from our ongoing campaign to study the optical properties of blazars on diverse timescales. We monitored the blazar S5 1803+78 quasi-simultaneously in $BVRI$ on 122 nights to investigate the optical properties of the source. Our data set includes a total of ∼2100 $BVRI$ frames collected from 2020 May to 2021 July using three ground-based optical telescopes, i.e., the 1.0 m RC telescope, 60 cm RC robotic telescope, and 0.5 m RC telescope in Turkey. During this monitoring period, the source brightness in the R band varied from 13.617 ± 0.009 to 15.888 ± 0.01. During our observation campaign, we observed the brightest flare for the blazar S5 174 1803+78 to date. The source started flaring around 2020 August 2 and this flaring lasted for 57 days. The blazar was in its brightest-ever state on 2020 August 25 with an R-band magnitude of 13.617. To investigate source properties in optical regimes during different brightness states, we performed our analysis on diverse timescales and also during the flare period. Studying blazars during their outburst state provides an opportunity to understand their variability, spectral behavior, color trends, and dominant emission mechanisms in much greater detail. This unprecedented flare is used to understand various characteristics of the source in detail from minute timescales to yearly timescales. Blazar emission during the outburst state is predominantly understood by relativistic shocks propagating through the jet. In general, during the flaring state nonthermal Doppler-boosted emission from relativistic jet plasma is dominant and is enhanced by the propagation of shocks in the flows (Blandford & Königl 1979).

Microvariability in blazar sources has gained special attention, partially because of the requirements of the very efficient particle acceleration and very fast energy dissipation mechanisms necessary to produce it. To study intraday variability during the flaring and nonflaring periods, we observed the source continuously in the R band for ∼1.5–4 hr on a total of 13 nights. To verify the presence of IDV in our source, we used a power-enhanced F-test and the ANOVA test, and only in two instances was the source found to be variable using both tests. During the flare period, we studied IDV on three days, i.e., 2020 August 30, August 31, and September 10. We did not find any significant variability on any of these nights. The source was variable on minute timescales on only two nights with variability amplitude of 7.47 and 10.10. However, the low duty cycle of the source could be due to the small observation spans. Gupta & Joshi (2005) extensively studied microvariability in a sample of AGN classes. One of the major findings was that ∼60%–65% of blazars are variable on intraday timescales when observed for <6 hr, whereas this fraction increases to ∼80%–85% when the blazars are monitored for more than 8 hr. Therefore, the duty cycle of our source may further increase if we increase the observation duration. On longer timescales, covering the entire monitoring duration, strong flux variations were seen in all optical bands.

Several detailed works in the literature have been dedicated to studying optical variability in AGNs to understand the location and size of emission regions, dominant particle acceleration mechanisms, the supermassive black hole (SMBH) mass, and various radiative processes in AGNs. The relativistic jet of blazars is pointed directly toward us, and thus their
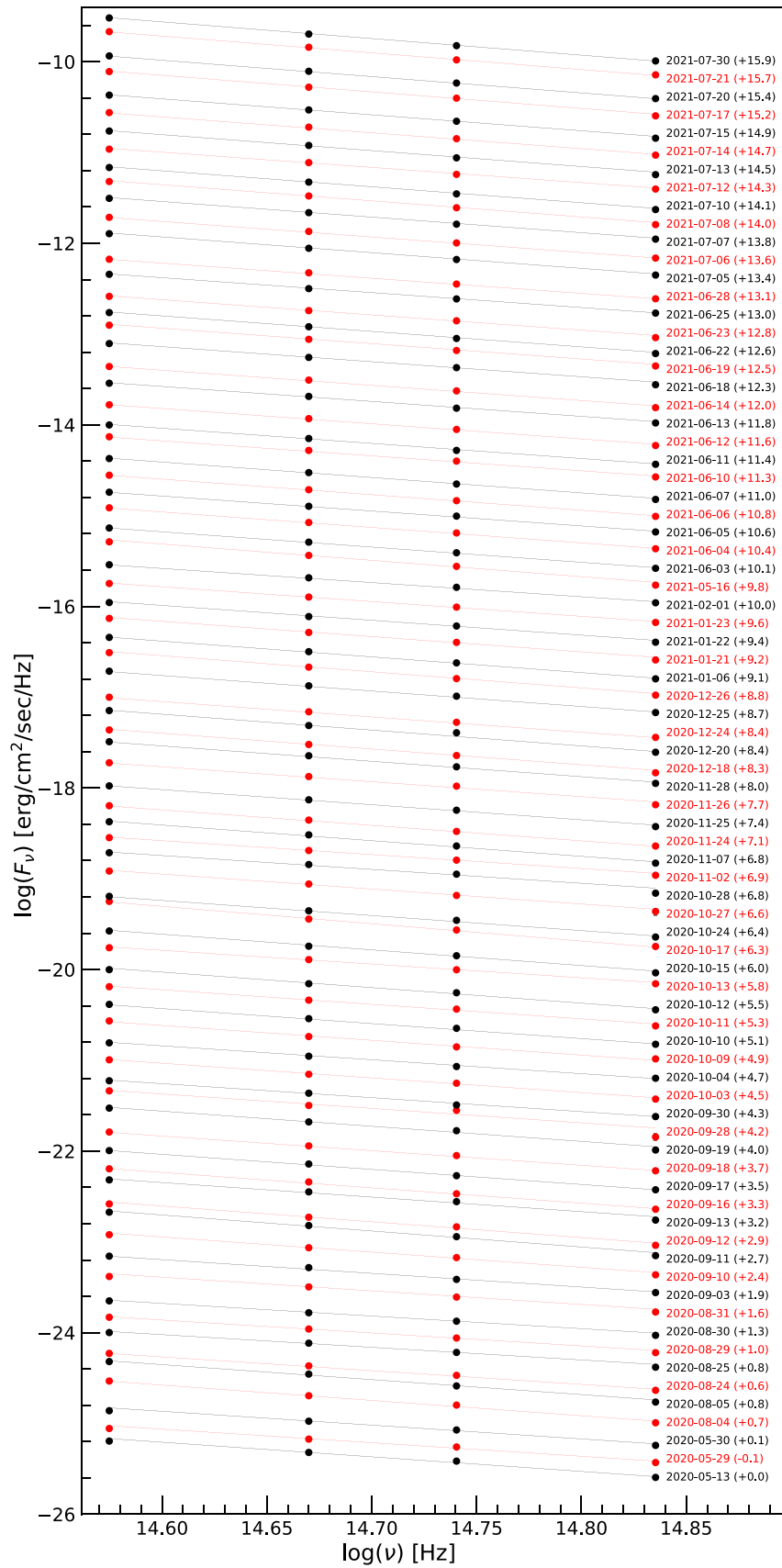
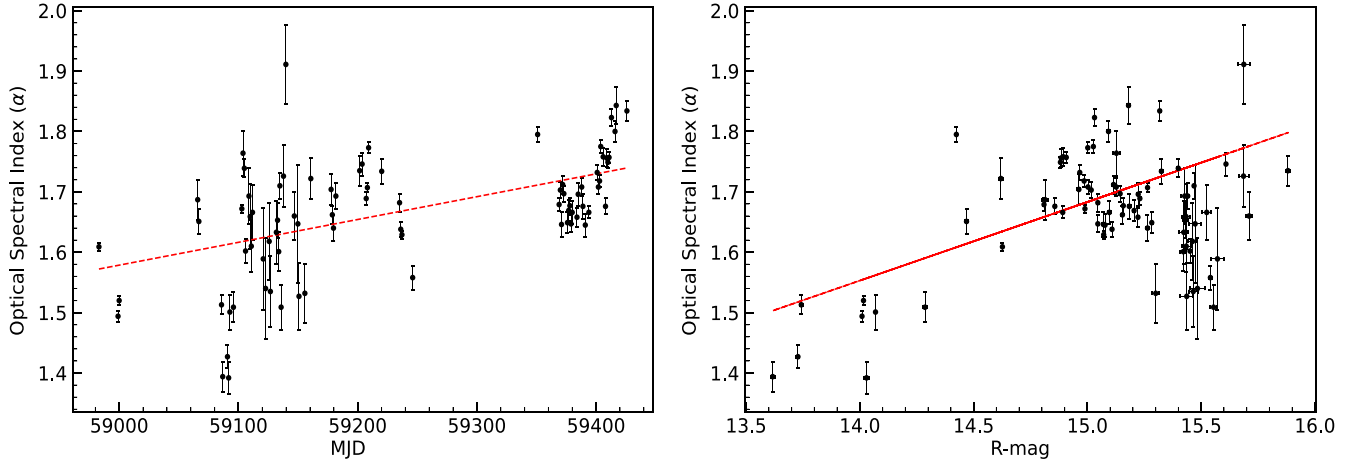**Figure 6.** SEDs of S5 1803+784 in *B*, *V*, *R*, and *I* bands.

Figure 7. Variation of optical spectral index of S5 1803+784 with respect to time (left) and *R* magnitude (right) during the entire monitoring period.

Table 5
Straight-line Fits to Optical SEDs of Blazar S5 1803+784

MJD	α	C	r	p	MJD	α	C	r	p
58,982.96772	1.609 ± 0.007	−1.715 ± 0.107	−0.995	4.770e-03	59,203.71728	1.746 ± 0.019	−0.096 ± 0.279	−0.993	7.325e-03
58,998.98042	1.494 ± 0.009	−3.150 ± 0.137	−0.994	5.688e-03	59,207.13390	1.689 ± 0.010	−0.789 ± 0.147	−1.000	7.659e-05
58,999.92728	1.520 ± 0.008	−2.774 ± 0.120	−0.995	4.932e-03	59,208.13391	1.707 ± 0.007	−0.539 ± 0.097	−0.999	6.084e-04
59,065.79383	1.687 ± 0.033	−0.647 ± 0.480	−0.998	2.163e-03	59,209.13391	1.773 ± 0.009	0.543 ± 0.128	−0.999	5.381e-04
59,066.79105	1.651 ± 0.020	−1.047 ± 0.294	−0.998	2.042e-03	59,220.13778	1.734 ± 0.021	−0.166 ± 0.303	−1.000	4.028e-04
59,085.77261	1.513 ± 0.016	−2.777 ± 0.239	−0.999	1.151e-03	59,235.11852	1.682 ± 0.015	−0.807 ± 0.215	−0.998	2.148e-03
59,086.76983	1.394 ± 0.025	−4.469 ± 0.373	−0.997	3.412e-03	59,236.11852	1.638 ± 0.012	−1.474 ± 0.169	−0.999	1.202e-03
59,090.76682	1.427 ± 0.019	−4.026 ± 0.283	−0.998	1.681e-03	59,237.11852	1.629 ± 0.007	−1.600 ± 0.108	−0.999	5.571e-04
59,091.76404	1.392 ± 0.026	−4.654 ± 0.383	−0.999	1.340e-03	59,246.10932	1.558 ± 0.020	−2.835 ± 0.296	−0.999	1.141e-03
59,092.78255	1.501 ± 0.029	−3.074 ± 0.420	−0.996	3.809e-03	59,350.92200	1.795 ± 0.013	1.094 ± 0.192	−0.996	3.519e-03
59,095.77343	1.509 ± 0.025	−3.064 ± 0.373	−0.998	1.730e-03	59,368.94119	1.679 ± 0.010	−0.765 ± 0.146	−1.000	3.195e-04
59,102.82033	1.672 ± 0.007	−0.934 ± 0.100	−0.997	2.870e-03	59,369.95820	1.703 ± 0.013	−0.496 ± 0.194	−1.000	2.758e-04
59,103.79566	1.764 ± 0.037	0.351 ± 0.547	−0.996	4.003e-03	59,370.95542	1.646 ± 0.021	−1.353 ± 0.307	−0.999	7.234e-04
59,104.91954	1.739 ± 0.015	−0.115 ± 0.223	−0.996	4.331e-03	59,371.95265	1.712 ± 0.015	−0.403 ± 0.215	−1.000	2.261e-04
59,105.92044	1.602 ± 0.020	−2.157 ± 0.291	−0.994	6.406e-03	59,372.94987	1.697 ± 0.013	−0.634 ± 0.191	−1.000	3.085e-04
59,108.78177	1.693 ± 0.047	−0.817 ± 0.693	−0.999	9.965e-04	59,375.94512	1.649 ± 0.017	−1.401 ± 0.255	−0.999	7.203e-04
59,109.77900	1.659 ± 0.054	−1.314 ± 0.785	−1.000	4.051e-04	59,376.94234	1.669 ± 0.017	−1.070 ± 0.243	−1.000	4.414e-04
59,110.77622	1.610 ± 0.043	−2.028 ± 0.624	−1.000	4.779e-04	59,377.93956	1.677 ± 0.013	−0.936 ± 0.187	−0.999	6.989e-04
59,111.77346	1.666 ± 0.046	−1.236 ± 0.670	−0.994	5.861e-03	59,378.93678	1.647 ± 0.014	−1.331 ± 0.212	−0.999	6.661e-04
59,120.74868	1.589 ± 0.084	−2.371 ± 1.229	−0.971	2.913e-02	59,379.93366	1.666 ± 0.019	−1.075 ± 0.272	−0.999	1.473e-03
59,122.74335	1.540 ± 0.084	−3.073 ± 1.230	−0.998	1.567e-03	59,383.92279	1.658 ± 0.016	−1.232 ± 0.237	−0.998	1.686e-03
59,125.78247	1.618 ± 0.064	−1.909 ± 0.940	−0.999	1.095e-03	59,384.92001	1.696 ± 0.019	−0.674 ± 0.280	−1.000	2.872e-04
59,126.77969	1.535 ± 0.059	−3.129 ± 0.858	−0.999	6.743e-04	59,387.90868	1.708 ± 0.015	−0.463 ± 0.222	−1.000	2.447e-04
59,131.76587	1.633 ± 0.052	−1.674 ± 0.766	−0.998	2.129e-03	59,388.90590	1.676 ± 0.021	−0.952 ± 0.309	−0.999	1.188e-03
59,132.77812	1.653 ± 0.029	−1.396 ± 0.419	−0.999	7.459e-04	59,390.90034	1.645 ± 0.019	−1.362 ± 0.280	−1.000	1.207e-05
59,133.77535	1.601 ± 0.032	−2.148 ± 0.475	−0.997	2.548e-03	59,393.89194	1.666 ± 0.010	−0.995 ± 0.149	−1.000	3.162e-04
59,134.72219	1.710 ± 0.022	−0.562 ± 0.319	−0.998	2.262e-03	59,400.87296	1.732 ± 0.012	−0.043 ± 0.181	−1.000	1.404e-04
59,135.76977	1.509 ± 0.037	−3.557 ± 0.545	−0.999	8.772e-04	59,401.87018	1.708 ± 0.012	−0.423 ± 0.172	−1.000	2.325e-04
59,137.76423	1.726 ± 0.051	−0.411 ± 0.745	−0.999	1.307e-03	59,402.87035	1.718 ± 0.010	−0.257 ± 0.141	−1.000	1.381e-04
59,139.75867	1.911 ± 0.065	2.297 ± 0.953	−1.000	4.625e-04	59,403.86758	1.775 ± 0.011	0.560 ± 0.160	−0.999	7.563e-04
59,146.82911	1.660 ± 0.040	−1.403 ± 0.591	−0.999	1.321e-03	59,405.86260	1.758 ± 0.015	0.365 ± 0.225	−1.000	2.136e-04
59,149.82111	1.647 ± 0.098	−1.502 ± 1.433	−0.999	1.444e-03	59,407.85704	1.676 ± 0.013	−0.827 ± 0.193	−1.000	4.930e-04
59,150.75872	1.527 ± 0.055	−3.250 ± 0.800	−0.992	7.907e-03	59,408.85369	1.756 ± 0.015	0.334 ± 0.220	−0.999	8.112e-04
59,155.69414	1.532 ± 0.049	−3.113 ± 0.714	−0.999	9.812e-04	59,409.85270	1.749 ± 0.009	0.227 ± 0.136	−1.000	4.583e-04
59,160.68115	1.722 ± 0.034	−0.067 ± 0.501	−0.998	2.233e-03	59,410.84807	1.757 ± 0.009	0.343 ± 0.130	−0.999	6.219e-04
59,177.69894	1.704 ± 0.025	−0.463 ± 0.368	−1.000	6.381e-05	59,412.84338	1.823 ± 0.014	1.266 ± 0.210	−0.999	7.346e-04
59,178.70550	1.662 ± 0.015	−1.153 ± 0.213	−0.999	9.858e-04	59,415.83563	1.800 ± 0.017	0.896 ± 0.253	−1.000	1.723e-05
59,179.70116	1.640 ± 0.022	−1.523 ± 0.323	−0.996	3.865e-03	59,416.83250	1.843 ± 0.031	1.490 ± 0.450	−1.000	2.485e-04
59,181.69795	1.693 ± 0.022	−0.819 ± 0.318	−0.999	9.028e-04	59,425.80553	1.834 ± 0.017	1.315 ± 0.255	−1.000	7.693e-05
59,201.66377	1.735 ± 0.025	−0.366 ± 0.360	−0.999	1.043e-03	⋯	⋯	⋯	⋯	⋯

Note. α = spectral index and C = intercept of $\log(F_\nu)$ against $\log(\nu)$; r = correlation coefficient; and p = null hypothesis probability.
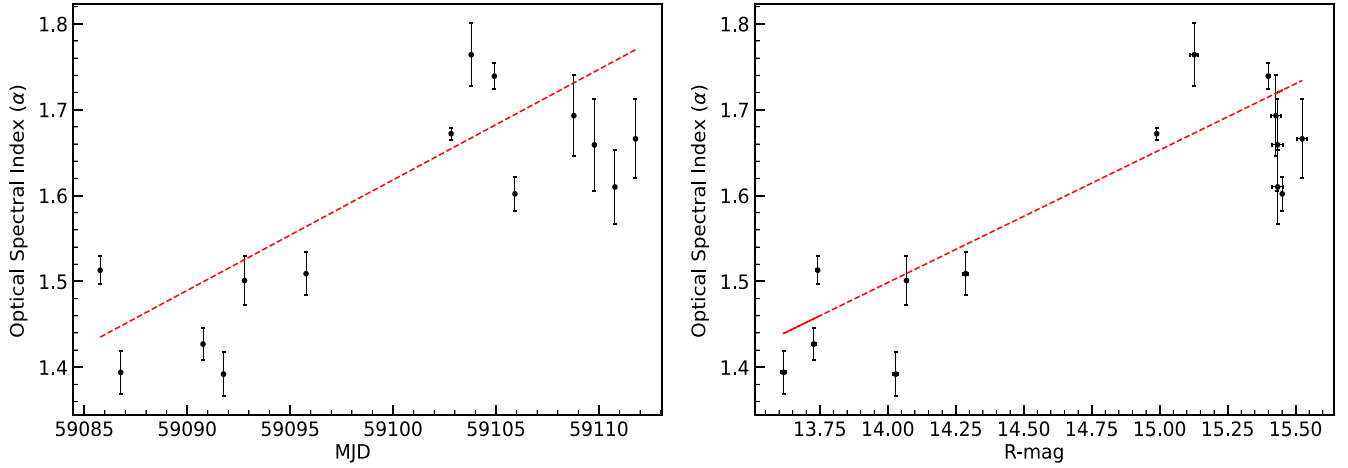
Figure 8. Variation of optical spectral index of S5 1803+784 with respect to time (left) and R magnitude (right) during the flaring period (MJD 59,085.77–MJD 59,111.77).

Table 6
Variation of Spectral Index with Time and R Magnitude during the Entire Monitoring Period

Parameters	m_2	c_2	r_2	p_2
α versus time	3.78e-04 ± 1.12e-05	−20.72 ± 0.66	0.54	2.39e-07
α versus R magnitude	1.30e-01 ± 4.08e-03	−0.27 ± 0.06	0.44	4.76e-05

Note. m_2 = slope and c_2 = intercept of α against time or R magnitude; r_2 = correlation coefficient; and p_2 = null hypothesis probability.

Table 7
Variation of Spectral Index with Time and R Magnitude during the Flaring Period (MJD 59,085.77–MJD 59,111.77)

Parameters	m_3	c_3	r_3	p_3
α versus time	1.29e-02 ± 6.97e-04	−759.05 ± 41.21	0.81	4.33e-04
α versus R magnitude	1.54e-01 ± 7.94e-03	−0.66 ± 0.12	0.87	5.75e-05

Note. m_3 = slope and c_3 = intercept of α against time or R magnitude; r_3 = correlation coefficient; and p_3 = null hypothesis probability.

emission at different frequencies mainly comes from the extragalactic jet. This makes blazars the best sources for studying jets, central SMBHs, and the accretion disk. Blazar variability is one such tool to understand the blazar structure. Variability could be due to intrinsic or extrinsic mechanisms. In the intrinsic mechanism scenario, flux variability is widely believed to occur due to particle injection and/or acceleration in a thin section within the jet, such as the jet base or the shock front. The propagation of multiple shocks can cause shock–shock interactions leading to an increase in magnetic field and the acceleration of particles. Changes in the magnetic field or electron density can cause flux changes in the source. These weak flux changes are greatly enhanced by extreme Doppler boosting, thus causing large changes in the observed flux and the timescale of variability. Another possible scenario for an intrinsic mechanism that can cause flux variability is magnetic reconnection (Böttcher & Baring 2019). In contrast, extrinsic mechanisms involve geometrical processes (due to a change in the orientation of the emission region with our line of sight), microlensing, and interstellar scintillation (Gopal-Krishna & Wiita 1992; Bignall et al. 2003; Raiteri et al. 2017).

Many studies in the past have shown different intraday variability behaviors in various classes of blazars, with BL Lacertae objects being comparatively less variable on intraday timescales (Gopal-Krishna et al. 2011). Fine-scale structures, such as inhomogeneities or bends in the base of jets, can cause intraday variability in the optical light curves of blazars when interacting with the shocks in jets. The Kelvin–Helmholtz instabilities responsible for these small-scale structures in the relativistic jets of BL Lacertae objects are prevented if the

axial magnetic field exceeds the critical magnetic field value, which is defined as (Romero 1995)

$$B_c = [4\pi n_e m_e c^2 (\Gamma^2 - 1)]^{1/2}\Gamma^{-1}, \qquad (4)$$

where n_e is the density, m_e is the rest mass of the electron, and Γ is the jet's bulk Lorentz factor. The stronger magnetic field of BL Lacertae objects such as our source S5 1803+784 would prevent the occurrence of small-scale instabilities, thus giving less pronounced microvariability.

According to the shock-in-jet scenario, the variability amplitude is larger at higher frequencies. This has been observed by many authors (e.g., Massaro et al. 1998; Papadakis et al. 2003; Dai et al. 2011; Agarwal et al. 2021b) and indicates that blazar spectra get steeper with a decrease in brightness and get flatter as brightness increases (Massaro et al. 1998; Papadakis et al. 2003). In many instances, the amplitude of variability of blazars at higher wavelengths is either comparable to or greater than that at lower wavelengths (Ghosh et al. 2000). We observed the same trend on longer timescales. The variability amplitudes for the blazar S5 1803+78 over the entire monitoring period in optical bands B, V, R, and I were found to be 238.481%, 234.842%, 227.060%, and 216.566%, respectively (Table 4). Such amplitude trends could be related to the synchrotron mechanisms responsible for optical radiation. According to the energy loss equation (under a constant magnetic field) we have $-d\gamma/dt \propto \gamma^2$ (where γ is the electron Lorentz factor) and $t_{sync} \propto 1/\gamma$, indicating the dissipation of a large amount of energy (by higher-energy electrons) as high-frequency photons could emerge in shorter timescales. This, therefore, causes any spectral changes to be observed first

in bluer wavelengths and then in redder ones with a certain delay. Moreover, this amplitude trend can be a hint toward the presence of BWB chromatism in the source on intraday timescales.

To further understand the spectral changes in the source, we generated optical SEDs using the quasi-simultaneous B-, V-, R-, and I-band data points corrected for Galactic extinction. We generated 79 such optical SEDs and they were found to be well defined by a simple power law. We then fitted these SEDs with a straight line to get the spectral indices. The spectral index during our observation period varied from 1.392 to 1.911 while the weighted mean spectral index was 1.673 ± 0.002. Our results were found to be in good agreement with Lawrence et al. (1996) and Nesci et al. (2021). The steep optical spectra of the source are consistent with synchrotron emission as the dominant process at optical frequencies along with the presence of relatively strong axial magnetic fields of the relativistic jet.

Analysis of the variation of spectral indices with time and R-band magnitudes during the whole monitoring period indicates the presence of a mildly detectable BWB trend ($r \sim 0.5$). During the flare, the source followed a much stronger BWB color behavior ($r \sim 0.9$). Several theories can interpret the mild BWB trend obtained during our long-term observations. According to Hawkins (2002), underlying host galaxy effects can cause color changes over time. But with one of their jets pointed toward the observer, BL Lacertae objects are weakly beamed and intrinsically weak. Therefore, the nonthermal Doppler-boosted emission from the relativistic jet powers the observed emission from BL Lacertae objects and swamps the light from the accretion disk, particularly during the active phase. Therefore, jet-based theoretical models can shed light on the flux and color variability results we have obtained. Moreover, as pointed out by Butuzova (2021), the presence or absence of the BWB trend on diverse timescales can be interpreted by different lifetimes of subcomponents with various Doppler factors and volumes.

Sun et al. (2014) studied timescale-dependent color variations. According to their model, the BWB trend is stronger for timescales <30 days, and it weakens on longer timescales of more than 100 days. Our results are also in agreement with this. As evident from Tables 6 and 7, the correlation coefficient value (r) varies from 0.87 (during the flare period of ~ 26 days[7]) to 0.44 (during the entire monitoring period of more than ~ 400 days).

The correlation between emissions at different frequencies can be used to infer the structure of the blazar, the various emission processes at work, and the location of emission regions. It is always difficult to detect time delays in optical wavelengths, due to small wavelength separations among different optical bands. Here, we studied the cross-correlation between different optical bands during the brightest flare of the source and also during the entire monitoring period using DCF analysis. Almost all combinations of optical frequencies in both cases gave strong correlation with a near-zero time lag, which suggests these emission regions are co-spatial. The flare is expected to start simultaneously in optical frequencies as the optical B, V, R, and I passbands are closely spaced. Therefore, short-timescale observations could possibly not detect time lags among these passbands. We also carried out a periodicity

search using four different methods: DACF, SF, WWZ, and LSP. To estimate the significance of the peaks, we followed Timmer & Koenig (1995). No significant periodicity was found on longer timescales spanning the period of 2020 May to 2021 July. Unevenly sampled observations make it difficult to search for periodicity in blazars. Any detection of quasiperiodicity can provide important clues on emission mechanisms occurring in the source and also help us in having a better understanding of the various theoretical models for blazars.

This work is part of an ongoing project focusing on understanding source behavior during a recent unprecedented flare of the source using dense optical observations. Due to the low cadence of multifrequency data, i.e., X-ray and γ-ray data, understanding source behavior on minute timescales was not feasible. Therefore, to investigate source behavior on diverse timescales during different states of the source, we focused on optical data here. Near-simultaneous multifrequency observations play an important role in understanding various problems of blazar physics. In this direction, observations of a large sample of blazars using 1–2 m class telescope facilities can prove to be very useful. Apart from S5 1803+78, we are observing a dozen γ-ray blazars using various small-aperture telescopes to get important leads in studying blazar physics and to confirm findings that already exist.

ORCID iDs

A. Agarwal ⓘ https://orcid.org/0000-0003-4682-5166
Ashwani Pandey ⓘ https://orcid.org/0000-0003-3820-0887
Avik Kumar Das ⓘ https://orcid.org/0000-0002-9526-0870

References

Abdo, A. A., Ackermann, M., Agudo, I., et al. 2010, ApJ, 716, 30
Acciari, V. A., Ansoldi, S., Antonelli, L. A., et al. 2021, MNRAS, 504, 1427
Agarwal, A., Cellone, S. A., Andruchow, I., et al. 2019, MNRAS, 488, 4093
Agarwal, A., & Gupta, A. C. 2015, MNRAS, 450, 541
Agarwal, A., Gupta, A. C., Bachev, R., et al. 2015, MNRAS, 451, 3882
Agarwal, A., Mihov, B., Andruchow, I., et al. 2021b, A&A, 645, A137
Agarwal, A., Rani, P., Prince, R., et al. 2021a, Galax, 9, 20
Bessell, M. S., Castelli, F., & Plez, B. 1998, A&A, 333, 231
Bignall, H. E., Jauncey, D. L., Lovell, J. E. J., et al. 2003, ApJ, 585, 653
Blandford, R. D., & Königl, A. 1979, ApJ, 232, 34
Böttcher, M. 2007, Ap&SS, 307, 69
Böttcher, M., & Baring, M. G. 2019, ApJ, 887, 133
Böttcher, M., Fultz, K., Aller, H. D., et al. 2009, ApJ, 694, 174
Butuzova, M. S. 2021, APh, 129, 102577
Cawthorne, T. V., Jorstad, S. G., & Marscher, A. P. 2013, ApJ, 772, 14

Cellone, S. A., Romero, G. E., & Araudo, A. T. 2007, MNRAS, 374, 357
Ciprini, S., Tosti, G., Raiteri, C. M., et al. 2003, A&A, 400, 487
Costamante, L., Ghisellini, G., Giommi, P., et al. 2001, A&A, 371, 512
Dai, Y., Wu, J., Zhu, Z.-H., Zhou, X., & Ma, J. 2011, AJ, 141, 65
de Diego, J. A. 2014, AJ, 148, 93
de Diego, J. A., Polednikova, J., Bongiovanni, A., et al. 2015, AJ, 150, 44
Dermer, C. D., & Schlickeiser, R. 1993, ApJ, 416, 458
Edelson, R. A., & Krolik, J. H. 1988, ApJ, 333, 646
Fan, J. H., Yang, J. H., Liu, Y., et al. 2016, ApJS, 226, 20
Fossati, G., Celotti, A., Ghisellini, G., & Maraschi, L. 1997, MNRAS, 289, 136
Foster, G. 1996, AJ, 112, 1709
Ghosh, K. K., Ramsey, B. D., Sadun, A. C., & Soundararajaperumal, S. 2000,
    ApJS, 127, 11
Gopal-Krishna, Goyal, A., Joshi, S., et al. 2011, MNRAS, 416, 101
Gopal-Krishna, & Wiita, P. J. 1992, A&A, 259, 109
Gupta, A. C., Fan, J. H., Bai, J. M., & Wagner, S. J. 2008, AJ, 135, 1384
Gupta, A. C., & Joshi, U. C. 2005, A&A, 440, 855
Hawkins, M. R. S. 2002, MNRAS, 329, 76
Heidt, J., & Wagner, S. J. 1996, A&A, 305, 42
Hovatta, T., Tornikoski, M., Lainela, M., et al. 2007, A&A, 469, 899
Kun, E., Karouzos, M., Gabányi, K. É., et al. 2018, MNRAS, 478, 359
Lawrence, C. R., Zucker, J. R., Readhead, A. C. S., et al. 1996, ApJS, 107, 541
Mannheim, K. 1993, A&A, 269, 67
Marscher, A. P., & Travis, J. P. 1996, A&AS, 120, 537
Massaro, E., Mantovani, F., Fanti, R., et al. 2001, A&A, 374, 435
Massaro, E., Nesci, R., Maesano, M., Montagni, F., & D'Alessio, F. 1998,
    MNRAS, 299, 47
Mastichiadis, A., & Kirk, J. G. 2002, PASA, 19, 138

Nesci, R., Cutini, S., Stanghellini, C., et al. 2021, MNRAS, 502, 6177
Nesci, R., Maselli, A., Montagni, F., & Sclavi, S. 2012, AcPol, 52, 39
Nesci, R., Massaro, E., Maesano, M., et al. 2002, AJ, 124, 53
Nilsson, K., Pursimo, T., Takalo, L. O., et al. 1999, PASP, 111, 1223
Pandey, A., Gupta, A. C., Damljanovic, G., et al. 2020a, MNRAS, 496,
    1430
Pandey, A., Gupta, A. C., Kurtanidze, S. O., et al. 2020b, ApJ, 890, 72
Pandey, A., Gupta, A. C., & Wiita, P. J. 2017, ApJ, 841, 123
Pandey, A., Gupta, A. C., Wiita, P. J., & Tiwari, S. N. 2019, ApJ, 871, 192
Papadakis, I. E., Boumis, P., Samaritakis, V., & Papamastorakis, J. 2003,
    A&A, 397, 565
Peng, C. Y., Ho, L. C., Impey, C. D., & Rix, H.-W. 2002, AJ, 124, 266
Polednikova, J., Ederoclite, A., de Diego, J. A., et al. 2016, MNRAS,
    460, 3950
Pursimo, T., Nilsson, K., Takalo, L. O., et al. 2002, A&A, 381, 810
Raiteri, C. M., Villata, M., Acosta-Pulido, J. A., et al. 2017, Natur, 552, 374
Rector, T. A., & Stocke, J. T. 2001, AJ, 122, 565
Romero, G. E. 1995, Ap&SS, 234, 49
Schneider, P., & Weiss, A. 1987, A&A, 171, 49
Sikora, M. 1994, ApJS, 90, 923
Sun, Y.-H., Wang, J.-X., Chen, X.-Y., & Zheng, Z.-Y. 2014, ApJ, 792, 54
Timmer, J., & Koenig, M. 1995, A&A, 300, 707
Urry, C. M., & Padovani, P. 1995, PASP, 107, 803
Valtonen, M. J., Lehto, H. J., Nilsson, K., et al. 2008, Natur, 452, 851
Wagner, S. J., & Witzel, A. 1995, ARA&A, 33, 163
Wiita, P. J. 1996, in ASP Conf. Ser. 110, Blazar Continuum Variability, ed.
    H. R. Miller, J. R. Webb, & J. C. Noble (San Francisco, CA: ASP), 42
Wu, J., Zhou, X., Ma, J., & Jiang, Z. 2011, MNRAS, 418, 1640